ELSEVIER

Journal of Nuclear Materials 296 (2001) 54–60

journal of nuclear materials

www.elsevier.com/locate/jnucmat

Section 2. Neutronics calculation and measurements of spallation produced gases

Radiation damage to the 316 stainless steel target container vessel at SNS

M.H. Barnett [a], M.S. Wechsler [a,*,1], D.J. Dudziak [a], L.K. Mansur [b], B.D. Murphy [b]

[a] *North Carolina State University, Raleigh, NC 27695-7900, USA*
[b] *Oak Ridge National Laboratory, Oak Ridge, TN 37831-6151, USA*

Abstract

In the past, our calculations of radiation damage (concentrations of displacements, helium atoms, and hydrogen atoms) to the 316 stainless steel (316SS) container vessel at the spallation neutron source (SNS) mercury target dealt with the average damage rates in a volume at the nose of the vessel. This paper describes an attempt to improve the accuracy of estimates of the damage rates at the center of the proton beam where the damage rates are expected to be the highest. Four series of calculations (Series I–IV) were conducted to determine the damage rates within volumes (tally volumes) that varied systematically in location in the vessel. This permitted extrapolation to the rates at the tip of the vessel nose ($Z = 0$) and at the center of the proton beam ($X = Y = 0$). The total damage rates due to protons and neutrons were found to be: 36 dpa/yr, 1400 appmHe/yr, and 20 000 appmH/yr. In addition, insight was gained into how the damage rates vary with position in the vessel nose and at locations further downstream in the vessel.

1. Introduction

The general design of the SNS spallation neutron source is described in its Conceptual Design Report [1]. Currently, the proton energy and current are considered to be 1 GeV and 2 mA, corresponding to a beam power of 2 MW. The spallation neutrons are produced when the protons impinge on the liquid mercury target material that is contained in a 316SS (Fe + 18 wt% Cr + 10 wt% Ni) vessel. The vessel has a multiwall structure consisting of four walls or shells, one inside the other (see [1, Fig. 5.3-6] or [2, Fig. 1]). Here, we concentrate on the innermost wall. The upstream end or nose of the wall has a half-cylindrical shape with cylinder axis in the Y-direction (Z = proton beam direction and X = vertical direction). The outer and inner surfaces of the half-cylinders have radii of 4.3 and 4.0 cm. The two surfaces are not concentric, and at the tip of the nose the thickness of the wall is 0.13 cm. The incident proton beam is contained within a 7×20 cm^2 rectangle perpendicular to the beam direction. The 2 mA current corresponds to 3.94×10^{23} protons per year or 1.25×10^{16} protons per second. The peak current density at the center of the beam is 0.224 A/m^2, which corresponds to 1.40×10^{14} protons per cm^{2}s. In the vertical or X-direction, the beam takes the shape of a Gaussian distribution with $2\sigma = 3.5$ cm, as shown in Fig. 1. In the horizontal direction, Y-axis, the current density is constant out to about $Y = \pm 8$ cm, and then it decreases to about 20% of its peak value at $Y = \pm 10$ cm (Fig. 2).

Earlier papers [2–5] have described the general approach to calculating displacement, helium and hydrogen production rates at spallation neutron sources. Average proton and neutron fluxes are determined in specific volumes. In addition, cross sections are calculated for the production of displacements, helium and hydrogen as a function of proton and neutron energy. The cross sections are then folded into the fluxes to yield production rates.

* Corresponding author. Tel.: +1-919 929 5193; fax: +1-919 933 6727.
E-mail address: wechsler@ncsu.edu (M.S. Wechsler).
[1] Present address: 106 Hunter Hill Place, Chapel Hill, NC 27514-9128, USA.

0022-3115/01/$ - see front matter
PII: S0022-3115(01)00499-8

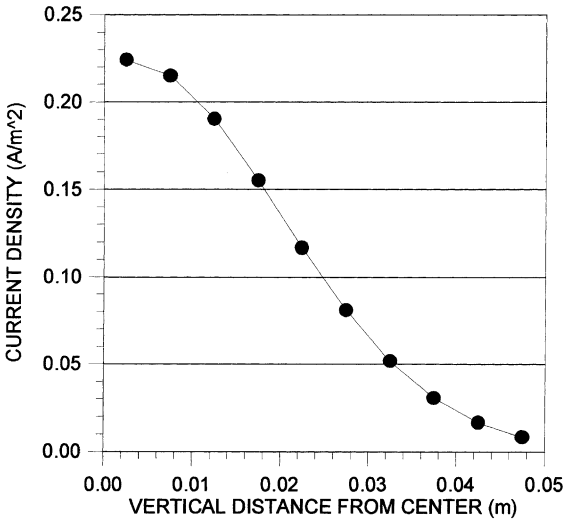

Fig. 1. Proton beam profile in the vertical (X)-direction.

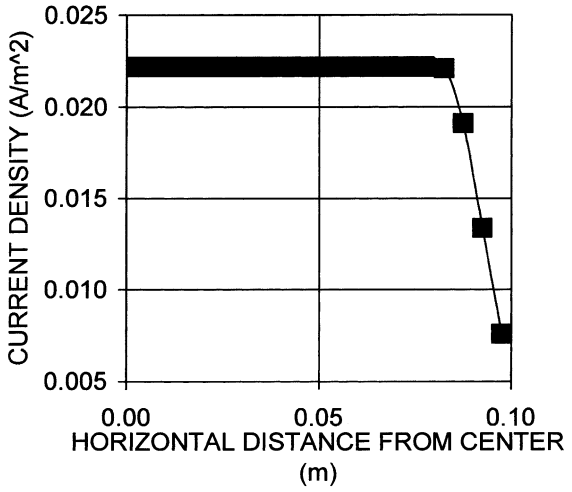

Fig. 2. Proton beam profile in the horizontal (Y)-direction.

2. Proton and neutron fluxes

The SNS target structure, including the four shells, Pb reflector, moderators, and neutron beam channels has been detailed in an MCNPX [6–8] SNS geometry file. We used this file to define various regions of interest in the geometry of the target vessel. The volumes of these regions were calculated, and the neutron and proton fluxes were determined by taking the track lengths within the volume per incident proton as tallied by MCNPX, dividing by the volume, and multiplying by the number of incident protons per unit time. For each tally (F4 tally in MCNP terminology [9,10]), 4×10^5 or 5×10^5 incident protons were run. MCNPX is the result of a merger of MCNP and LAHET [11].

Table 1 indicates the Series I–IV tally regions over which the fluxes were determined. Series I–III consist of regions in the vessel nose. For these, each entry in Table 1 specifies a rectangle in the X–Y plane with its center at $X = Y = 0$. The corresponding tally volume is given by the volume of 316SS that is intercepted at the nose upon projection of the rectangle in the Z-direction. In the column for Series I, the rectangles increase in both X- and Y-dimensions in going down the column, but the $Y : X$ ratio is kept at 3:1. The rectangle of smallest area, 0.5×1.5 cm^2, is designated below as the smallest box (SB). In the column for Series II, the X-dimension of the rectangles increases in going down the column, but the Y-dimension is fixed at 3 cm. Similarly, in the column for Series III, the Y-dimension increases, but the X-dimension is fixed at 1 cm. For Series IV, the tally volumes consisted of the 316SS metal lying between X–Y planes in the Z-ranges indicated in the fourth column of Table 1. We chose to set $Z = 0$ at the tip of the nose of the innermost shell; this point corresponds to $Z = -20.52$ cm in the SNS geometry file.

The tally volume corresponding to the first Z-range, $Z = 0$–0.52 cm is designed tally volume 1 (TV1) illustrated in Fig. 3. The curves $A'E'$ and AE represent the outer and inner surfaces of the vessel nose, respectively, and the centers of the circles are at C′ (at $Z = 4.30$ cm) and C (at $Z = 4.13$ cm), respectively. The radii of the half-cylinders are 4.3 and 4.0 cm, respectively. Based on the incident current densities shown in Figs. 1 and 2, the ratio of the maximum current density (J_0) to average current density ($\langle J \rangle$) incident on TV1 is calculated to be about 1.6. Based on the MCNPX track length tally, the calculated average proton flux of all energies in TV1 is calculated to be 0.996×10^{14} p/cm^2 s. The corresponding proton flux for SB is 1.52×10^{14} p/cm^2 s, which gives a SB/TV1 ratio of 1.53. This is consistent with the incident $J_0/\langle J \rangle = 1.6$, since the current density at the top and bottom edges of the SB rectangle (i.e., at $X = \pm 0.25$ cm with $2\sigma = 3.5$ cm) divided by J_0 is about 0.99. In other words, the SB box should see an average current density that is only slightly less than that at the center of the proton beam. The neutron fluxes of all energies for TV1 and SB are found to be 6.86×10^{14} and 8.78×10^{14} n/cm^2 s. Radiation damage rates in TV1 are discussed in [5].

Fig. 4 shows the average flux of protons and neutrons in tally volumes for Series I, Table 1, as a function of the rectangle areas in the X–Y plane presented to the proton beam. The fluxes for TV1 and SB are also shown. The fractional decrease in the proton flux is greater than for the neutron flux. This is especially true for the proton flux when the rectangle dimensions exceed the 7×20 cm^2 dimensions of the incident proton beam profile in the X–Y plane.

Table 1
Box dimensions for Series I, II, III, and IV flux tallies

Series I, X–Y expansion (cm × cm)	Series II, X expansion (cm × cm)	Series III, Y expansion (cm × cm)	Series IV, Z survey (Z-range (cm))
0.5 × 1.5	0.5 × 3	1 × 1.5	0–0.52
1 × 3	1 × 3	1 × 3	0.52–1.52
1.5 × 4.5	1.5 × 3	1 × 6	1.52–2.52
2 × 6	2 × 3	1 × 9	2.52–3.52
2.5 × 7.5	2.5 × 3	1 × 12	3.52–4.52
3 × 9	3 × 3	1 × 15	4.52–5.52
3.5 × 10.5	3.5 × 3	1 × 18	5.52–6.52
4 × 12	4 × 3	1 × 21	6.52–7.52
4.5 × 13.5	4.5 × 3	1 × 24	7.52–8.52
5 × 15	5 × 3	1 × 27	8.52–9.52
5.5 × 16.5	5.5 × 3		9.52–10.52
6 × 18	6 × 3		10.52–11.52
6.5 × 19.5	6.5 × 3		11.52–12.52
7 × 21	7 × 3		12.52–13.52
7.5 × 22.5	7.5 × 3		13.52–14.52
8 × 24	8 × 3		14.52–15.52
8.5 × 25.5	8.5 × 3		15.52–17.52
9 × 27	9 × 3		17.52–19.52
			19.52–21.52
			21.52–23.52
			23.52–25.52
			25.52–30.52
			30.52–35.52
			35.52–40.52
			40.52–50.52
			50.52–60.52
			60.52–70.52

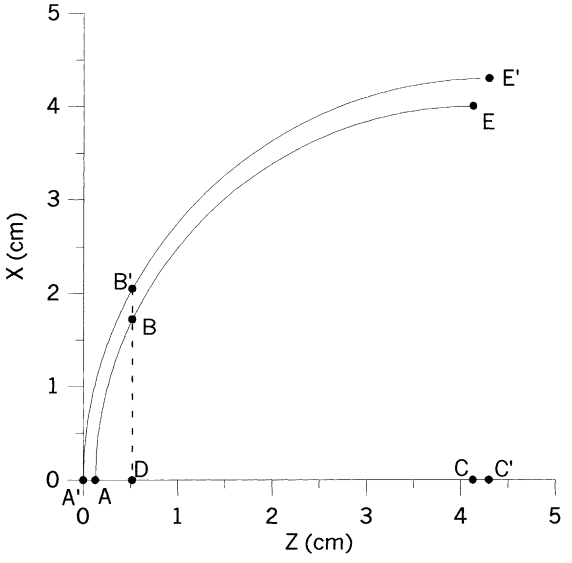

Fig. 3. $A'B'BA$ is the upper half (for $X > 0$) of TV1. $A'D = 0.52$ cm, $B'D = 2.05$ cm.

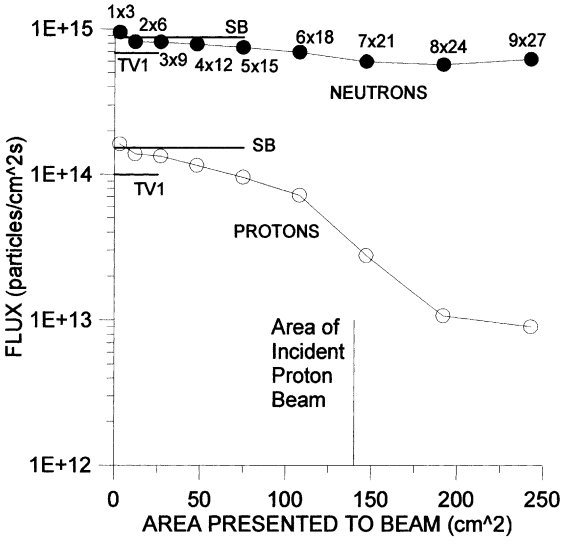

Fig. 4. Average proton and neutron flux for tally volumes for Series I, Table 1, vs the areas of the rectangles in the X–Y plane presented to the incident proton beam. The fluxes for TV1 and SB are also shown.

3. Damage rates

In this paper, attention is concentrated on displacement production rates, although corresponding results for helium and hydrogen are also summarized below. As mentioned above, the damage rates are determined by folding the fluxes into the production cross sections for displacements, He, and H. In most cases, this was done by setting up an energy bin structure, determining the integral flux of protons and neutrons for each energy bin, multiplying by the cross section for the energy bin midpoint, and, for the total damage rates, summing the products over all energies. The displacement cross sections used are those given in [5, Fig. 3]. For energies, E, below 20 MeV, the displacement cross sections stem from SPECTER [12]; for $20 < E < 150$ MeV, the LA150 [13] cross sections were used; and for 150 MeV $< E$, we employed LAHET [11] in the default mode which uses the RAL evaporation–fission model [14,15].

The displacement production rate for protons, neutrons, and protons + neutrons for Series I, Table 1, is shown in Fig. 5 as a function of rectangle area. The contribution of neutrons is greater than that of protons over the entire range of areas. The displacement rates are averages over the tally volume in each case, and they decrease as more volume is included at larger X-distances where the incident current density is lower (Fig. 1). The decreases are roughly linear out to about 150 cm^2, i.e., out to the 7×21 cm^2 case. Since the incident beam profile is 7×21 cm^2, the curves are fairly level past this point.

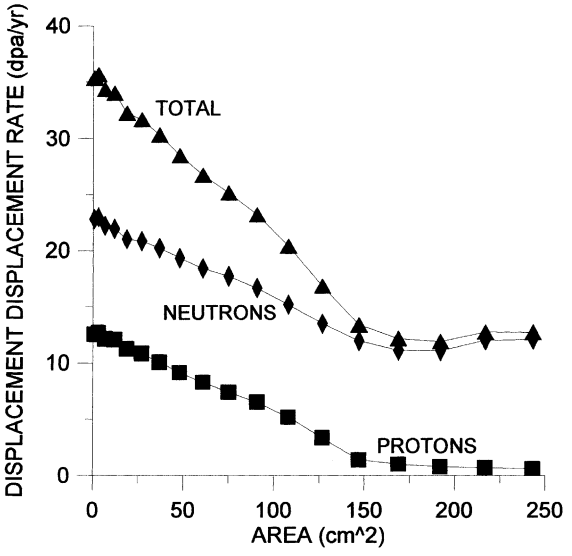

Fig. 5. Displacement production rate vs rectangle area for Series I, Table 1.

The Series II survey of tally volumes (second column, Table 1) covers 18 rectangles with X (vertical)-heights that vary from 0.5 to 9 cm and Y (horizontal)-dimension all 3 cm wide. The incident proton current density in the X-direction follows a Gaussian distribution with $2\sigma = 3.5$ cm (Fig. 1). The proton and neutron differential fluxes in each of the tally volumes were determined as described above for Series I, and folded into the displacement, helium, and hydrogen cross sections. The resulting displacement production rate is shown in Fig. 6. Again, displacement production is greater for neutrons than for protons. The least-squares fit to the proton-induced displacement rate gave an intercept at zero half-height of 13.2 ± 0.2 dpa/yr and a Gaussian sigma of $\sigma = 1.88 \pm 0.02$ cm, to be compared with $\sigma = 1.75$ cm for the incident proton profile along X (Fig. 1). The fit to the Gaussian is reasonably good, although the three points at half-heights of 0.25, 0.5, and 0.75 cm (where the statistical error in determining the fluxes is greatest) lie below the fitted curve.

For Series III (third column, Table 1), the expansion is in the X-direction with the rectangle widths varying from 1.5 to 27 cm, while the heights along X are fixed at 1 cm. Fig. 7 shows once again that displacement production is greater for neutrons than for protons. Since the incident proton current density is constant out to a half-width of about 8 cm (Fig. 2), we see that the proton curve in Fig. 7 is quite constant out to this distance and then it begins to decrease as areas are added that receive no protons from the incident beam. The curve for

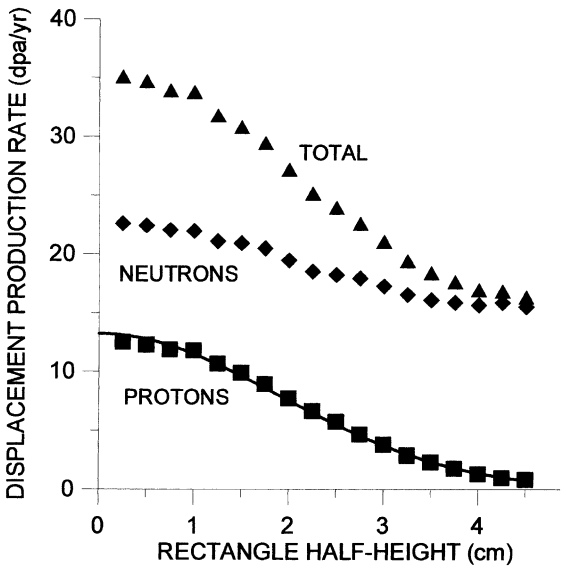

Fig. 6. Displacement production rate vs rectangle half-height along the vertical (X)-direction for the 18 rectangles for Series II, Table 1. The width along the horizontal (Y)-direction is fixed at 3 cm. The curve for the protons is a least-squares best fit to a Gaussian distribution.

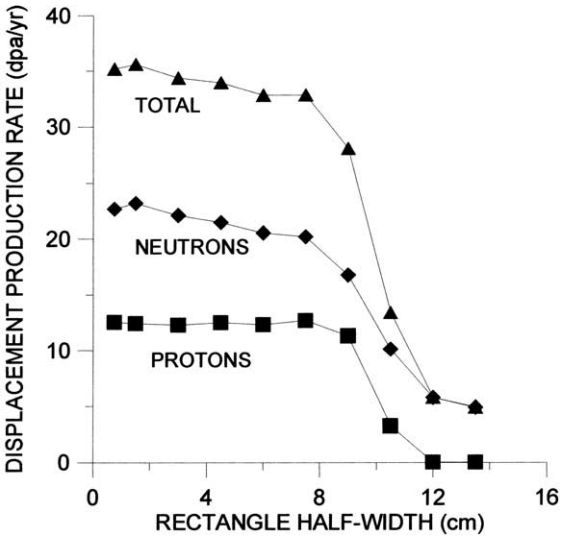

Fig. 7. Displacement production rate vs rectangle half-width along the horizontal (Y)-direction for the 10 rectangles for Series III, Table 1. The height along the X-direction is fixed at 1 cm.

neutrons in Fig. 7 follows somewhat the same pattern, although there is a slight decrease inside of $Y = \pm 8$ cm, and the decrease in displacement rate outside of that range is more gradual than for protons.

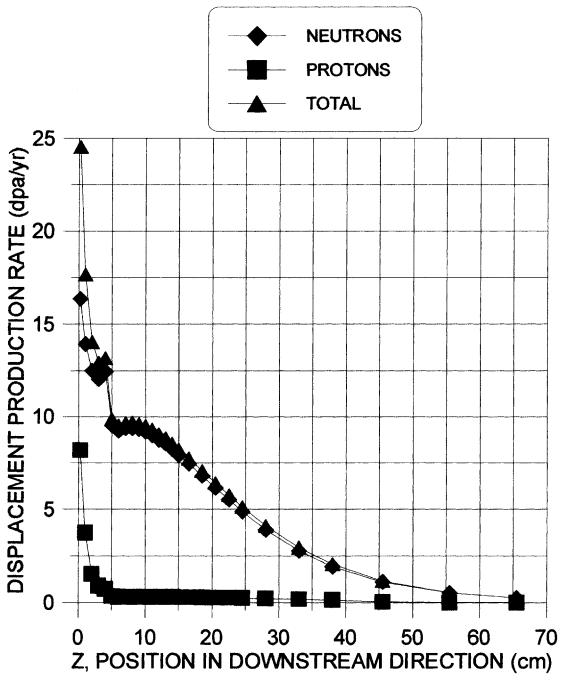

Fig. 8. Displacement production rate vs Z-midpoint for Series IV, Table 1.

In Table 1, Series IV (Z survey) differs from I, II, and III in that it does not consist in an expansion from one item to the next one down the list. Instead, each item in the fourth column of Table 1 represents a separate and distinct tally volume that does not include any volume also in another item. Series IV indicates Z-ranges in which various amounts of 316SS are located, over which the fluxes and damage rates are averaged. For the first five Z-ranges in the fourth column of Table 1, i.e., for $Z < 4.52$ cm, all of the 316SS is at the half-cylindrical nose. Further downstream the intercepted metal consists of the sides, top, and bottom of the vessel. Fig. 8 gives the displacement production rate as a function of the midpoint of the Z-range. The proton- and neutron-induced displacement rates decrease for the first five Z-ranges as the intercepted metal in the nose moves to higher and higher absolute X-values. Then, past about $Z = 4.5$ cm the nose is no longer intercepted and all of the intercepted metal is at the sides, top, and bottom of the vessel. The displacement rate due to protons then falls close to zero. The neutron rate falls more gradually and reaches near zero only at Z-values near 60 or 70 cm.

4. Discussion

The Z-range in Series IV closest to the tip of the nose extends from $Z = 0$ to 0.52 cm. The average displacement rates for that tally volume, centered at $Z = 0.26$ cm, are 16.4 dpa/yr for neutrons and 8.2 dpa/yr for protons, giving a total of 24.6 dpa/yr (Fig. 8). However, these average rates refer to our TV1, which extends from $X = +2.05$ cm (point B' in Fig. 3) to $X = -2.05$ cm, i.e. it extends into a region where the incident proton current density is reduced because of the Gaussian shape of the current density profile along X (Fig. 1).

To obtain an evaluation of peak damage rates at $X = Y = 0$, we examine the results of Series I, II, and III, as shown in Figs. 5–7. Estimates of the short extrapolations to the ordinate axis give damage production rates as shown in Table 2. For displacement rates, the extrapolations for Series I, II, and III give essentially the same results, namely, 23, 13, and 36 dpa/yr for neutrons, protons, and total, respectively. For the He and H production rates, the rates for the three series differ slightly, as shown in Table 2. Roughly, the He rates at X = Y = 0 appear to be: For He, 130, 1300, and 1400 appmHe/yr for neutrons, protons, and total, respectively, and for H, the corresponding values are 1800, 18 000, and 20 000 appmH/yr, respectively, where the totals are rounded off. For the totals, one obtains the approximate ratios: 40 appmHe/dpa and 14 atoms of H per atom of He. Also, for He and H production, we note that the proton-induced damage rates are about a factor of ten greater than the neutron-induced rates.

Table 2
Damage rates from Series I, II, III

	Neutrons	Protons	Total
Displacements (dpa/yr)			
Series I	23	13	36
Series II	23	13	36
Series III	23	13	36
He (appmHe/yr)			
Series I	129	1290	1420[a]
Series II	130	1260	1390
Series III	130	1200	1330
H (appmH/yr)			
Series I	1800	20000	21800
Series II	1800	17000	18800
Series III	1820	16100	17900[a]

[a] Values rounded off.

In addition to the results of calculations such as those discussed above, experimental observations are emerging that are likely to be of considerable help in the assessment of the significance of radiation effects on materials for spallation neutron sources. These investigations include results on spallation-irradiated materials. For further information, the reader is referred to the papers by Maloy et al. [16] and Pawel et al. [17] in the proceeding of a recent conference and by Farrell [18] in these Proceedings.

Acknowledgements

Lowell Charlton made a significant contribution to the performance of this work. We regret deeply that he is no longer with us.

References

[1] Conceptual Design Report, National Spallation Neutron Source, vols. 1&2, NSNS/CDR-2/V1 and NSNS/CDR-2/V2, Oak Ridge National Laboratory, Oak Ridge, TN, May 1997.
[2] M.S. Wechsler, M.H. Barnett, D.J. Dudziak, L.K. Mansur, L.A. Charlton, J. M. Barnes, J.O. Johnson, in: M.S. Wechsler, L.K. Mansur, C.L. Snead, W.F. Sommer, (Eds.), Materials for Spallation Neutron Sources, The Minerals, Metals, and Materials Society (TMS), Warrendale, PA, 1998, p. 23.
[3] L.A. Charlton, L.K. Mansur, M.H. Barnett, R.K. Corzine, D.J. Dudziak, M.S. Wechsler, in: Proceedings of the Second International Topical Meeting on Nuclear Applications of Accelerator Technology (AccApp'98), American Nuclear Society, La Grange Park, IL, 1998, p. 247.
[4] M.S. Wechsler, M.H. Barnett, D.J. Dudziak, R.K. Corzine, W.F. Sommer, E.J. Pitcher, P.D. Ferguson, L.K. Mansur, K. Farrell, L.A. Charlton, J.M. Barnes, J.O. Johnson, in: Proceedings of the Topical Meeting on Nuclear Applications of Accelerator Technology, American Nuclear Society, La Grange Park, IL, 1997, p. 21.
[5] M.H. Barnett, M.S. Wechsler, D.J. Dudziak, R.K. Corzine, L.A. Charlton, L.K. Mansur, in: Proceedings of the Third International Topical Meeting on Nuclear Applications of Accelerator Technology (AccApp'99), American Nuclear Society, La Grange Park, IL, 1999, p. 555.
[6] H.G. Hughes, K.J. Adams, M.B. Chadwick, J.C. Comly. L.J. Fox, H.W. Egdorf, S.C. Frankle, J.S. Hendricks, R.C. Little, R. MacFarlane, R.E. Prael, L.S. Waters, M.C. White, P.G. Young, F.X. Gallmeier, E.C. Snow, in: Second International Topical Meeting on Nuclear Applications of Accelerator Technology (AccApp'98), American Nuclear Society, La Grange Park, IL, 1998, p. 281.
[7] H.G. Hughes, K.J. Adams, M.B. Chadwick, J.C. Comly, S.C. Frankle, J.S. Hendricks, R.C. Little, R.E. Prael, L.S. Waters, P.G. Young, Jr., in: Proceedings of the Topical Meeting on Nuclear Applications of Accelerator Technology (AccApp'97), American Nuclear Society, La Grange Park, IL, 1997, p. 213.
[8] H.G. Hughes, R.E. Prael, R.C. Little, MCNPX – The LAHET/MCNP Code Merger, Technical Report, XTM-RN (U) 97-012, Los Alamos National Laboratory, Los Alamos, NM, April 1997.
[9] J.F. Briesmeister (Ed.), MCNP – A General Monte Carlo Code for Neutron and Photon Transport, Version 4B, Los Alamos National Laboratory, March 1997 (See also, Report LA-12625-M, Los Alamos National Laboratory, Los Alamos, NM, 1997).
[10] Monte Carlo N-Particle Transport Code System, MCNP4B2, RSICC Computer Code Collection, CCC-660, Radiation Safety Information Computation Center, Oak Ridge National Laboratory, Oak Ridge, TN, 1998.
[11] R.E. Prael, H. Lichtenstein, User Guide to LCS: The LAHET Code System, LA-UR 89-3014, Radiation Transpost Group, Los Alamos National Laboratory, Los Alamos, NM, September 1989.
[12] L.R. Greenwood, R.K. Smither, SPECTER: Neutron Damage Calculations for Materials Irradiations, ANL/FPP/TM-197, Argonne National Laboratory, January, 1985.
[13] M.B. Chadwick, S.C. Frankle, R.C. Little, P.G. Young, in: Proceedings on the Topical Meeting on Nuclear Applications of Accelerator Technology, American Nuclear Society, La Grange Park, IL, 1997, p. 175.
[14] F. Atchison, in: Targets for Neutron Beam Spallation Sources, Jül-Conf-34, Kernforschungsanlage Jülich GmbH, January 1980.
[15] R.E. Prael, A Review of Physics Models in the LAHET Code, in: Proceedings of a Specialists' Meeting, Issyles-Moulineaux, France, 30 May–1 June 1994, Intermediate Energy Nuclear Data: Models and Codes, OECD, 1994, p. 145.
[16] S.A. Maloy, M.R. James, W.F. Sommer, P. Ferguson, G. Willcutt, D. Alexander, M.R. Louthan, Jr., M.L. Hamilton, L. Snead, M.A. Sokolov, in: Proceedings of the Third International Topical Meeting on Nuclear Applications of

Accelerator Technology, (AccApp'99), American Nuclear Society, La Grange Park, IL, 1999, p. 541.
[17] S.J. Pawel, J.R. DiStefano, L.K. Mansur, K.Farrell, J.P. Strizak, T.S. Byun, in: Proceedings of the Third International Topical Meeting on Nuclear Applications of Accelerator Technology, (AccApp'99), American Nuclear Society, La Grange Park, IL, 1999, p. 117.
[18] K. Farrell, T.S. Byun, these Proceedings, p. 129.